Nonlinear wave interactions in bubble layers

S. Karpov and A. Prosperetti[a)]
Department of Mechanical Engineering, The Johns Hopkins University, Baltimore, Maryland 21218

L. Ostrovsky[b)]
Zel Technologies/NOAA ETL, Boulder, Colorado 80305

(Received 2 May 2001; accepted for publication 30 November 2002)

Due to the large compressibility of gas bubbles, layers of a bubbly liquid surrounded by pure liquid exhibit many resonances that can give rise to a strongly nonlinear behavior even for relatively low-level excitation. In an earlier paper [Druzhinin *et al.*, J. Acoust. Soc. Am. **100**, 3570 (1996)] it was pointed out that, by exciting the bubbly layer in correspondence of two resonant modes, so chosen that the difference frequency also corresponds to a resonant mode, it might be possible to achieve an efficient parametric generation of a low-frequency signal. The earlier work made use of a simplified model for the bubbly liquid that ignored the dissipation and dispersion introduced by the bubbles. Here a more realistic description of the bubble behavior is used to study the nonlinear oscillations of a bubble layer under both single- and dual-frequency excitation. It is found that a difference-frequency power of the order of 1% can be generated with incident pressure amplitudes of the order of 50 kPa or so. It appears that similar phenomena would occur in other systems, such as porous waterlike or rubberlike media. © *2003 Acoustical Society of America.*
[DOI: 10.1121/1.1539519]

PACS numbers: 43.25.Lj, 43.25.Gf, 43.25.Jh [MFH]

I. INTRODUCTION

The high compressibility of a bubbly mixture causes significant nonlinear effects to arise even at relatively low pressure amplitudes. For this reason, several authors have considered the possibility of using such multiphase systems as active media in parametric arrays (Zabolotskaya and Soluyan, 1973; Kustov *et al.*, 1982; Ostrovsky *et al.*, 1998). The practical realization of this idea has not been very successful due to the use of a mixture of bubble sizes containing resonant bubbles at the incident frequency: the large losses that accompany bubble oscillations near resonance severely diminished the energy available for the parametric effect.

In an earlier paper (Druzhinin *et al.*, 1996) we suggested that the problem could be addressed in a novel way by exploiting the resonances of bubbly liquid layers. It was argued that, by adjusting the bubble size and the operating frequencies so that the desired low-frequency output correspond to layer resonances, it should be possible to operate efficiently while remaining far away from the individual bubble resonance: the result would be an increased efficiency of low-frequency generation and a moderate energy loss. Although promising, it should be noted that the practical realization of this concept requires the generation of bubbles smaller than the resonant radius at the frequencies of interest which, depending on the specifics of the required system, may not be an easy task.

Our earlier work demonstrated the validity of this expectation in principle, but had a preliminary nature in that isothermal gas behavior and a quasi-equilibrium dependence of the bubble radius on the external pressure were assumed. Furthermore, in the presence of the saw-tooth shock wave structure that develops even at moderate pressure amplitudes, the accuracy of the numerical method used in that work was questionable. It is the purpose of this paper to improve on the earlier analysis of the problem, both in the mathematical model and in the numerical treatment. While, unlike the earlier work, the complexity of the model prevents us from obtaining analytic results, the numerical simulations confirm the practical potential of the suggested arrangement.

A schematic representation of the situation studied in this paper is shown in Fig. 1: a one-dimensional layer of liquid containing gas bubbles is located between $x=0$ and $x=L$ and is excited by a plane wave normally incident from the left. As a result of this excitation, a reflected wave at the left of the layer and a transmitted wave at the right are generated.

Some further analysis and preliminary experiments on the low-frequency sound generation in such an arrangement were presented in Ostrovsky *et al.* (1998). The results were however somewhat inconclusive as the layer was resonant only for the difference frequency of the two incident waves, both of which had frequencies close to the individual bubble frequency and, therefore, were strongly dissipated.

II. MATHEMATICAL MODEL

We consider the one-dimensional problem sketched in Fig. 1. The mathematical model of the bubbly liquid consists of the continuity equation

$$\frac{1}{\rho_l c_l^2}\frac{\partial P}{\partial t}+\frac{\partial u}{\partial x}=\frac{\partial \beta}{\partial t}, \tag{1}$$

[a)]Also at Faculty of Applied Physics and Twente Institute of Mechanics, University of Twente, AE 7500 Enschede, The Netherlands, and Burgerscentrum, The Netherlands. Address correspondence to Johns Hopkins address. Electronic mail: prosperetti@jhu.edu
[b)]Also at Institute of Applied Physics, Nizhny Novgorod, Russia.

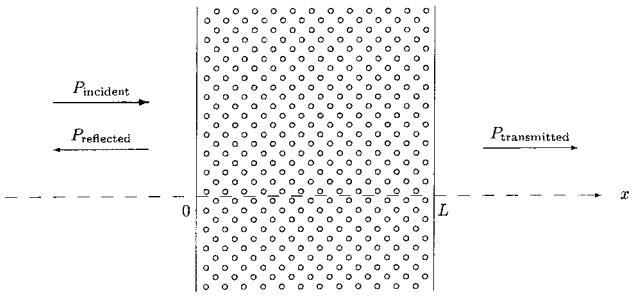

FIG. 1. Schematic representation of the one-dimensional bubble layer excited by a normally incident plane wave from the left.

in which ρ_l and c_l are the density and sound speed of the pure liquid and P and u are the average mixture pressure and velocity, and of the momentum equation

$$\rho_l \frac{\partial u}{\partial t} + \frac{\partial P}{\partial x} = 0. \tag{2}$$

This model is essentially that of Kogarko (1964) and van Wijngaarden (1968) except that, as pointed out by Caflisch *et al.* (1985), the convective term of the material derivative can be omitted due to the assumed smallness of the gas volume fraction β; additional considerations on this point are given in Watanabe and Prosperetti (1994), and further applications of this and similar models can be found e.g., in Zabolotskaya (1977), Kuznetsov *et al.* (1978), Gasenko *et al.* (1979), Nigmatulin (1991), Akhatov *et al.* (1994), Naugolnykh and Ostrovsky (1998), Colonius *et al.* (2000), and many others. Buoyancy effects are neglected in (2) due to the smallness of the acoustic time scale compared with the time evolution of the bubble layer. The volume fraction is given by

$$\beta(x,t) = \tfrac{4}{3}\pi R^3(x,t) n, \tag{3}$$

where $R(x,t)$ is the instantaneous radius of the bubbles contained in a small volume centered around x and n is the bubble number density. In the same assumption $\beta \ll 1$ under which (1) and (2) hold, the bubble number density n can be taken as independent of time; for simplicity, we further assume it to be spatially uniform. The expression (3) can be readily extended to a distribution of bubble sizes by inserting in the right-hand side an integral over the probability distribution of the bubble radii (Zhang and Prosperetti, 1994; Prosperetti, 2001) but, for simplicity, here we assume that all bubbles have the same radius. Generally speaking, if the size distribution is such that all the bubbles have a resonance frequency greater than those of interest, one would not expect very different results (see, e.g., Naugolnykh and Ostrovsky, 1998). On the other hand, if a significant fraction of resonant or near-resonant bubbles were present, dispersion would be very different, dissipation greatly increased, and the phenomena that we discuss strongly and adversely affected.

In spite of its appearance, the previous model retains a strong nonlinearity in the manner in which R is calculated. Again on the basis of the smallness of β, for this purpose we use the Rayleigh–Plesset equation of bubble dynamics (see, e.g., Plesset and Prosperetti, 1977; Prosperetti, 1991; Feng and Leal, 1997):

$$R\frac{\partial^2 R}{\partial t^2} + \frac{3}{2}\left(\frac{\partial R}{\partial t}\right)^2 = \frac{1}{\rho_l}\left(p - P - \frac{2\sigma}{R} - \frac{4\mu}{R}\frac{\partial R}{\partial t}\right). \tag{4}$$

Here p is the bubble internal pressure (approximated by the gas pressure, the small vapor contribution being neglected), σ is the surface tension coefficient, and μ is the liquid viscosity. For an isolated bubble, the ambient pressure P appearing in (4) is to be identified with the pressure at the location of the bubble if the bubble were absent. In a dilute mixture the bubbles are subject to the averaged field and P should be taken as the average pressure appearing in the momentum equation (2) (see, e.g., Caflisch *et al.*, 1985; Zhang and Prosperetti, 1994). As before, in (4) we omit the convective term of the material derivatives of R.

In writing (3) and (4) we have implicitly taken the bubble to be spherical, ignoring the distortion due to gravity, flow, and bubble–bubble interaction. This we do for simplicity and with little loss of accuracy since shape modes couple inefficiently to pressure perturbations when the spherical shape is stable. We have also neglected the corrections due to liquid compressibility (see, e.g., Prosperetti and Lezzi, 1986) which we had included in the early calculations for this paper but found to have a very small influence on the results [see Prosperetti (1984) for a comparison of the various damping mechanisms].

In order to close the system a relationship between the gas pressure p and bubble radius R is needed. This point has been treated at length in earlier papers (Prosperetti, 1991; Watanabe and Prosperetti, 1994). Suffice it to say that we approximate the gas pressure inside each bubble as spatially uniform, which leads to

$$\frac{\partial p}{\partial t} = \frac{3}{R}\left[(\gamma - 1)k\frac{\partial T}{\partial r}\bigg|_R - \gamma p\frac{\partial R}{\partial t}\right], \tag{5}$$

where T is the local gas temperature to be found from

$$\frac{\gamma}{\gamma - 1}\frac{p}{T}\left(\frac{\partial T}{\partial t} + v\frac{\partial T}{\partial r}\right) = \dot{p} + \frac{1}{r^2}\frac{\partial}{\partial r}\left(kr^2\frac{\partial T}{\partial r}\right), \tag{6}$$

with

$$v = \frac{1}{\gamma p}\left[(\gamma - 1)k\frac{\partial T}{\partial r} - \frac{1}{3}r\dot{p}\right]. \tag{7}$$

In these equations γ and $k = k(T)$ are the ratio of specific heats and thermal conductivity of the gas and r is the radial coordinate measured from the center of the bubble. As shown in Kamath *et al.* (1993), at the surface of the bubble, a suitable boundary condition for (6) is

$$T(R,t) = T_\infty, \tag{8}$$

where T_∞ is the undisturbed liquid temperature. It should be noted that, inside the bubble centered at x, the temperature field T depends on r as well as t and, hence, in principle, the set of equations (5)–(7) must be solved at all spatial locations in the layer.

In Druzhinin *et al.* (1996) we considered a much simpler model of the bubble behavior that was obtained from (4) by assuming an instantaneous equilibrium between internal and external pressures and ignoring viscosity and surface tension so that $p=P$; in addition, the bubble internal pressure was related to the radius by a polytropic assumption so that Eqs. (1) and (2) were closed by the simple relation

$$p_0\left(\frac{R_0}{R}\right)^{3\kappa_p}=P, \tag{9}$$

with κ_p a polytropic index. While the neglect of viscosity and surface tension is not very limiting for bubble sizes above a few tens of micrometers, the neglect of inertia on the left-hand side of (4) restricts the validity of this quasi-equilibrium model to frequencies much lower than the bubble resonance frequency. In this limit, in most parameter regions of interest, the bubbles behave isothermally so that Eq. (9) is justified with $\kappa_p=1$. Outside this very restricted domain of validity, however, the model of our earlier paper cannot be expected to be accurate.

A model intermediate between the quasi-equilibrium and complete models can be formulated by using, in the Rayleigh–Plesset equation (4), the polytropic relation (9) in place of (5) for the bubble internal pressure. This model, termed *polytropic* in the following, accounts for the inertia of the bubble radial motion, but not for the strongly dissipative thermal effects.

A. Boundary conditions

As the layer compresses and expands under the action of an incident pressure wave, the planes defining its boundaries will move normal to themselves. If the gas volume fraction is small, by the same argument that enables us to neglect the convective term in the material derivatives, we may disregard this effect and approximate the layer boundaries as fixed in space. As shown in Druzhinin *et al.* (1996), this approximation permits a great simplification of the problem.

Indeed, since the medium outside the bubble layer can be regarded as linear and is nondispersive, one may assume that the incident, reflected, and transmitted waves have the form

$$\begin{aligned} &P_{\rm inc}=P_i(x-c_l t), \quad P_{\rm trans}=P_t(x-c_l t),\\ &P_{\rm ref}=P_r(x+c_l t). \end{aligned} \tag{10}$$

At the layer boundaries the pressure should be continuous so that if, as before, P denotes the pressure in the layer,

$$P_i(0,t)+P_r(0,t)=P(0,t), \quad P(L,t)=P_t(L,t). \tag{11}$$

The velocity or, equivalently, the pressure gradients should also be continuous which, at $x=0$, gives

$$\frac{\partial P_i}{\partial x}+\frac{\partial P_r}{\partial x}=\frac{\partial P}{\partial x}. \tag{12}$$

By virtue of the particular form (10) of the functional dependence on x and t of P_i and P_r, the spatial derivatives are readily related to time derivatives and, upon taking the time derivative of (11), we can eliminate $\partial P_r/\partial t$. The result is the condition

$$\frac{\partial P}{\partial t}-c_l\frac{\partial P}{\partial x}=2\frac{\partial P_i}{\partial t} \quad \text{at } x=0. \tag{13}$$

Proceeding similarly at the right boundary we find

$$\frac{\partial P}{\partial t}+c_l\frac{\partial P}{\partial x}=0 \quad \text{at } x=L. \tag{14}$$

Because of this argument, the problem is reduced to solving the equations of Sec. II subject to the conditions (13) and (14) at $x=0$ and $x=L$. After the pressure P inside the bubble layer is determined, the reflected and transmitted waves are found from (11).

III. LINEAR RESULTS

For a better understanding of the material that follows, it is useful to summarize here some results of the linear analysis of the previous model.

As shown in Commander and Prosperetti (1989), for linear pressure perturbations the model of the previous section gives the following dispersion relation for monochromatic pressure waves with a time dependence proportional to $\exp(i\omega t)$ and wave number κ in a bubbly liquid:

$$\frac{\kappa^2}{\omega^2}=\frac{1}{c_l^2}+\frac{3\beta_0/R_0^2}{\omega_0^2-\omega^2+2ib\omega}. \tag{15}$$

A relation of this type has been derived by many authors starting from several similar models (see, e.g., Carstensen and Foldy, 1947; Clay and Medwin, 1977; Waterman and Truell, 1961; Twersky, 1962; Omta, 1987; d'Agostino and Brennen, 1988; Nigmatulin, 1991; Medwin and Clay, 1997). Here

$$\beta_0=\tfrac{4}{3}\pi R_0^3 n \tag{16}$$

is the gas volume fraction at equilibrium, $\omega_0/2\pi$ is the effective undamped resonance frequency of the bubbles, and b is the effective damping parameter; these quantities depend on the driving frequency ω and are given by

$$\omega_0^2=\frac{p_0}{\rho_l R_0^2}\left(3\kappa_l-\frac{2\sigma}{R_0 p_0}\right), \quad \kappa_l=\frac{1}{3}\,\mathrm{Re}\,\Phi, \tag{17}$$

$$b=\frac{2\mu_l}{\rho_l R_0^2}+\frac{p_0}{2\rho_l R_0^2\omega}\,\mathrm{Im}\,\Phi, \tag{18}$$

where κ_l is the linear-theory value of the polytropic index which is calculated from the complex function Φ defined by (Prosperetti, 1991)

$$\Phi=\frac{3\gamma}{1-3(\gamma-1)iz[(i/z)^{1/2}\coth(i/z)^{1/2}-1]}, \tag{19}$$

with $z=D/\omega R_0^2$, in which D is the gas thermal diffusivity. The ratio $c_m=\omega/\kappa$ is the phase velocity of the wave which (15) shows to be complex: the imaginary part describes the attenuation of the wave in the bubbly mixture due to the energy losses in the bubbles. In a water–air system viscous losses, described by the first term on the right-hand side of (18), are much smaller than the thermal ones except for bubble radii in the micrometer range. If liquid compressibility effects were retained in (4), an acoustic loss contribution

$b_{ac}=\omega^2 R_0/(2c_l)$ would be added to the right-hand side of (18); this term is also small for ω below the bubble resonance frequency ω_0.

For the quasi-equilibrium model of Eq. (9) the relation corresponding to (15) is

$$\frac{\kappa^2}{\omega^2}=\frac{1}{c_l^2}+\frac{\beta_0\rho_l}{\kappa_p P_\infty}, \tag{20}$$

where P_∞ is the undisturbed pressure in the liquid. This relation demonstrates the extreme sensitivity of the effective speed of sound κ/ω to the gas concentration; for example, in water $\rho_l c_l^2/P_\infty \simeq 2.25\times 10^4$ and, with $\kappa_p=1$ and $\beta=10^{-3}$, we have from (20) $c_l/c_m \simeq 5$.

For a monochromatic wave with unit amplitude normally incident on a bubble layer of thickness L, it is easy to show that the amplitudes of the transmitted and reflected waves, $A_{\rm tr}$ and $A_{\rm ref}$, are given by standard acoustic relations (see, e.g., Pierce, 1989, Secs. 3–7; Commander and Prosperetti, 1989)

$$A_{\rm tr}=\frac{\exp(i\omega L/c_l)}{\cos(\kappa L)+\frac{1}{2}i[\omega/(\kappa c_l)+\kappa c_l/\omega]\sin(\kappa L)}, \tag{21}$$

$$A_{\rm ref}=\frac{\frac{1}{2}i[\omega/(\kappa c_l)-\kappa c_l/\omega]\sin(\kappa L)}{\cos(\kappa L)+\frac{1}{2}i[\omega/(\kappa c_l)+\kappa c_l/\omega]\sin(\kappa L)}. \tag{22}$$

The corresponding results for the quasi-equilibrium model are conveniently written in the following form:

$$A_{\rm tr}=\frac{4A}{(A+1)^2-(A-1)^2\exp(-2iA\omega L/c_l)}, \tag{23}$$

$$A_{\rm ref}=\frac{(A^2-1)[\exp(-2iA\omega L/c_l)-1]}{(A+1)^2-(A-1)^2\exp(-2iA\omega L/c_l)}, \tag{24}$$

where the nondimensional parameter A is defined by

$$A=\frac{c_l}{c_m}=\sqrt{1+\frac{\rho_l\beta_0 c_l^2}{P_\infty\kappa_p}} \tag{25}$$

with the second equality following from (20). Equations (23) and (24) give a simple estimate of the resonance frequencies of the incident wave:

$$\omega_n=\frac{n\pi c_l}{AL}, \quad n=1,2,\ldots. \tag{26}$$

This estimate can be refined by calculating numerically the maxima and minima of the moduli of $A_{\rm tr}$ and $A_{\rm ref}$ given by (21) and (22).

IV. NUMERICAL METHOD

The problem to be solved can be decomposed in two components, the integration of the continuity and momentum equations in the bubbly liquid, and the calculation of the temperature inside the bubbles. While these two components are coupled, their nature is very different and so must be their numerical treatment.

In view of the strong nonlinear effects in the bubble layer, steep waveforms develop in the system. To avoid the well-known numerical oscillations that can arise in these conditions, we use the total variation diminishing method of Harten (1983), the implementation of which is now briefly described. It is convenient to use dimensionless variables defined according to

$$\begin{aligned} &x'=\frac{x}{L}, \quad t'=\frac{c_l t}{L}, \quad u'=\frac{\rho_l c_l}{P_\infty}u,\\ &P'=\frac{P}{P_\infty}-1, \quad \beta'=\frac{\beta}{\beta_0}, \end{aligned} \tag{27}$$

but we drop the primes for convenience.

The continuity and momentum equations (1) and (2) may be compactly written as

$$\frac{\partial \mathbf{w}}{\partial t}+\frac{\partial \mathbf{F}}{\partial x}=\frac{\rho_l\beta_0 c_l^2}{P_\infty}\mathbf{b}, \tag{28}$$

where the vectors $\mathbf{w}$, $\mathbf{F}$, and $\mathbf{b}$ are given by

$$\mathbf{w}=\begin{vmatrix} P \\ u \end{vmatrix}, \quad \mathbf{F}=\begin{vmatrix} u \\ P \end{vmatrix}, \quad \mathbf{b}=\begin{vmatrix} \partial\beta/\partial t \\ 0 \end{vmatrix}. \tag{29}$$

This system is discretized explicitly in time and in space as

$$\frac{\mathbf{w}_i^{n+1}-\mathbf{w}_i^n}{\Delta t}+\frac{\hat{\mathbf{F}}_{i+1/2}^n-\hat{\mathbf{F}}_{i-1/2}^n}{\Delta x}=\frac{\rho_l\beta_0 c_l^2}{P_\infty}\mathbf{b}_i^{n+1/2}, \tag{30}$$

where superscripts indicate time levels and subscripts spatial nodes. The modified fluxes $\hat{\mathbf{F}}$ are given by the following expression:

$$\begin{aligned} \hat{\mathbf{F}}_{i+1/2}=&\frac{1}{2}(\mathbf{F}_{i+1}+\mathbf{F}_i)\\ &+\frac{s}{2}\sum_{l=1}^{2}[g_i^{(l)}+g_{i+1}^{(l)}-\alpha_{i+1/2}^{(l)}Q(sa^{(l)}+\eta_{i+1/2}^{(l)})]\mathbf{R}^{(l)}, \end{aligned} \tag{31}$$

where $s=c_l\Delta t/\Delta x$ is the Courant number and

$$\mathbf{R}^{(1)}=\begin{vmatrix} 1 \\ 1 \end{vmatrix}, \quad \mathbf{R}^{(2)}=\begin{vmatrix} 1 \\ -1 \end{vmatrix}, \quad a^{(1)}=1, \quad a^{(2)}=-1, \tag{32}$$

$$\begin{aligned} \alpha_{i+1/2}^{(1)}&=\tfrac{1}{2}(P_{i+1}-P_i+u_{i+1}-u_i),\\ \alpha_{i+1/2}^{(2)}&=\tfrac{1}{2}(P_{i+1}-P_i-u_{i+1}+u_i), \end{aligned} \tag{33}$$

$$\eta_{i+1/2}^{(l)}=\begin{cases} (g_{i+1}^{(l)}-g_i^{(l)})/\alpha_{i+1/2}^{(l)} & \text{if } \alpha_{i+1/2}^{(l)}\neq 0,\\ 0 \quad \text{if } \alpha_{i+1/2}^{(l)}=0. \end{cases} \tag{34}$$

The function Q is defined by

$$Q(y)=\begin{cases} y^2/(4\epsilon)+\epsilon, & \text{for } |y|<2\epsilon,\\ |y|, & \text{for } |y|\geqslant 2\epsilon, \end{cases} \tag{35}$$

with $\epsilon=0.1$, and plays the role of an artificial viscosity. Furthermore,

$$g_i^{(l)}=\begin{cases} \min(|[Q(s)-s^2]\alpha_{i+1/2}^{(l)}|,|[Q(s)-s^2]\alpha_{i-1/2}^{(l)}|)\\ \qquad \text{if } \alpha_{i+1/2}^{(l)}\alpha_{i-1/2}^{(l)}\geqslant 0,\\ 0 \quad \alpha_{i+1/2}^{(l)}\alpha_{i-1/2}^{(l)}<0. \end{cases} \tag{36}$$

The terms in the summation in (31) are a correction to the components of the flux $\mathbf{F}$ along the characteristic directions,

which are introduced to account for the discretization error and guarantee second-order accuracy in space.

The time integration is a variant of a predictor-corrector method abbreviated so as to result in a faster execution without significant loss of accuracy. Briefly, the procedure is as follows. Suppose that everything is known at time level t^n. At all interior nodes we generate a preliminary estimate of the pressure $\tilde{P}^{n+1}$ at time level $t^{n+1}=t^n+\Delta t$ from (30) in which $(\partial_t\beta)^n$ is used in the vector **b** on the right-hand side (here and in the following, tildes denote provisional estimated values at time t^{n+1}.) With this updated pressure we calculate new values of $(\partial_t^2\tilde{R})^{n+1}$ and $(\partial_t\tilde{R})^{n+1}$ and use an approximation to the trapezoidal rule in the form

$$R^{n+1}=R^n+\tfrac{1}{2}\Delta t[(\partial_t R)^n+(\partial_t\tilde{R})^{n+1}], \tag{37}$$

and similarly for all the other variables. In executing this step, in principle it would be necessary to update the time derivative of the bubble pressure (5) as well, which would however significantly slow down the calculation. We found that simply using the value $\partial_t p|^n$ does not lead to a significant loss of accuracy.

After a variable transformation that fixes the bubble boundary, the energy equation in the gas (6) is turned into a set of ordinary differential equations in time by the Galerkin spectral method described in Kamath and Prosperetti (1989). The temperature is expanded over a set of even Chebyshev polynomials; the number of polynomials used in the expansion varies in time according to the procedure given in Kamath and Prosperetti (1989).

To generate the numerical results that follow we have typically used between 800 and 3200 spatial nodes per wavelength depending on the amplitude and the volume fraction: stronger incident waves lead to shock formation the resolution of which requires more nodes. The appropriate number of nodes was chosen by successively refining the grid until the results stabilized. For each level of discretization the time step Δt was chosen such that the Courant number was less than 0.2.

It is clear from the preceding description that the problem is solved as an initial-value problem. The time necessary to reach a steady state depends on the driving amplitude and the value of the parameter A. For weak excitation one typically needs about $20L/\lambda_m$ cycles, where λ_m is the wavelength in the bubbly mixture. For larger amplitudes dissipation is stronger and the numerical constant of 20 can be considerably reduced (Druzhinin *et al.*, 1996).

V. RESULTS: SINGLE-FREQUENCY EXCITATION

In all the examples that follow we use the physical properties of an air–water system at standard conditions. Specifically, we take $P_\infty=100$ kPa, $\rho_l=10^3$ kg/m^3, $c_l=1.5\times10^3$ m/s, and $\mu_l=10^{-3}$ N s/m^2, $\gamma=1.4$, $\sigma=0.07$ N/m; the air thermal conductivity is calculated from $k(T)=A_K T+B_K$ with $A_K=5.528\times10^{-5}$ J/(m s K^2) and $B_K=1.165\times10^{-2}$ J/(m s K), which provides a good fit to the data in the range 200 K$<T<$3000 K. The width of the bubble layer is taken to be $L=0.1$ m and the coupling parameter A defined in Eq. (25), evaluated for $\kappa_p=1$, is taken to be $\sqrt{31}\simeq5.57$, which corresponds to a bubble volume fraction $\beta_0=0.133\%$. Furthermore, we estimate the bubbly layer lowest mode ω_1 from (26) with $n=1$ and $\kappa_p=1$.

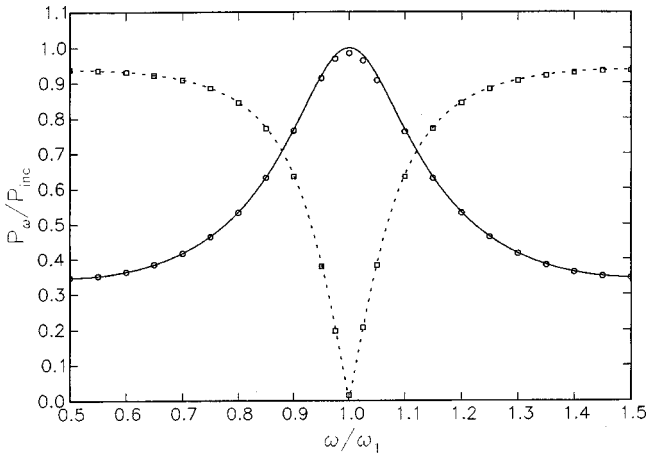

FIG. 2. Pressure amplitudes of the component at the incident wave frequency ω for the transmitted (circles) and reflected (squares) waves as functions of the incident frequency ω normalized by the first linear eigenfrequency of the layer according to the quasi-equilibrium model, $\omega_1/2\pi=1.347$ kHz; the solid and dotted lines are the linear results given in Eqs. (23) and (24). The incident wave amplitude $P_{\rm inc}/P_\infty=0.05$ is smaller than the threshold value for shock formation given by (38). The gas volume fraction is $\beta_0=0.133\%$, the ambient pressure $P_\infty=100$ kPa, the liquid density $\rho_l=10^3$ kg/m^3, the liquid speed of sound $c_l=1.5\times10^3$ m/s, the liquid viscosity $\mu_l=10^{-3}$ N s/m^2, the gas adiabatic index $\gamma=1.4$, the surface tension coefficient $\sigma=0.07$ N/m, and the width of bubble layer $L=0.1$ m.

Before turning to the results of the complete model, it is useful to study those given by the quasi-equilibrium model (9) for which the earlier results of Druzhinin *et al.* (1996), as well as the analytical ones of Sec. III, are available; clearly, the predictions of the quasi-equilibrium model are independent of the bubble radius.

A. Quasi-equilibrium model

Druzhinin *et al.* (1996) give the following criterion for the threshold amplitude of an incident monochromatic wave that leads to shock formation in the layer:

$$\frac{P_{\rm inc}^{\rm th}}{P_\infty}=\frac{4J_2(2)}{\pi J_1(1)}\frac{1}{n\sqrt{A^2-1}}, \tag{38}$$

where $J_{1,2}$ are Bessel functions, and it is assumed that the incident frequency corresponds to the nth resonance frequency of the layer. For $A=\sqrt{31}$, $n=1$, and isothermal oscillations, this relation gives a value of 0.18. Thus, in order to start with the linear regime, we consider first a case with an incident wave amplitude $P_{\rm inc}/P_\infty=0.05$. Figure 2 shows the transmitted (circles) and reflected (squares) amplitudes as functions of the ratio ω/ω_1 of the incident frequency to the lowest layer eigenfrequency which, here, is $\omega_1/2\pi=1.347$ kHz as given by (26). The amplitudes shown are for the components at the same frequency as the incident wave, which are found by taking the Fourier transforms of the total transmitted and reflected waves; the relative power of the higher-frequency components is smaller than 0.0004. In the figure the lines are the analytical results (23) and (24). The agreement is excellent, which suggests that the numerical

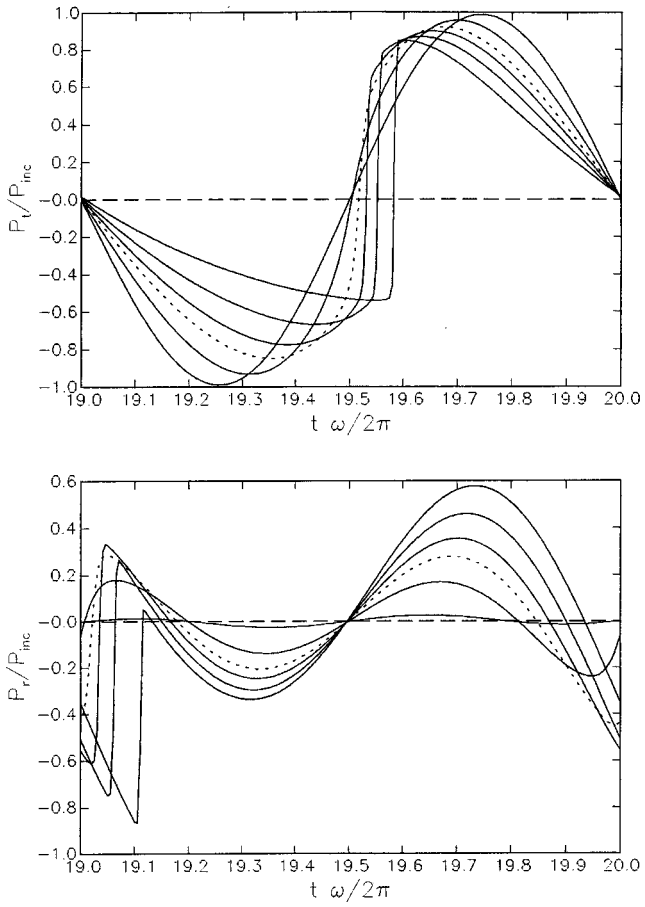

FIG. 3. Steady-state shape of transmitted (upper panel) and reflected waves for different amplitudes of the incident wave, $P_{\rm inc}/P_\infty=0.01$, 0.1, 0.2 (dotted), 0.3, 0.5, 0.9 according to the quasi-equilibrium model. The frequency of the incident wave is equal to the first linear eigenfrequency of the layer $\omega=\omega_1$, with $\omega_1/2\pi=1.347$ kHz. The gas volume fraction is $\beta_0=0.133\%$, the ambient pressure $P_\infty=100$ kPa, the liquid density $\rho_l=10^3$ kg/m^3, the liquid speed of sound $c_l=1.5\times10^3$ m/s, the liquid viscosity $\mu_l=10^{-3}$ N s/m^2, the gas adiabatic index $\gamma=1.4$, the surface tension coefficient $\sigma=0.07$ N/m, and the width of bubble layer $L=0.1$ m.

method is accurate and so is the computer code that implements it.

As the amplitude of the incident wave increases, nonlinear effects eventually lead to shock formation as demonstrated in Fig. 3, which shows the normalized transmitted (upper panel) and reflected waves at steady state for $P_{\rm inc}/P_\infty=0.01$, 0.1, 0.2 (dotted line), 0.3, 0.5, and 0.9; these waveforms are shown during the 20th cycle, by which time steady state has been reached. The results for $P_{\rm inc}/P_\infty=0.2$ are singled out using a dotted line because (38) gives a value of 0.18 for the shock-wave threshold, which is seen to be in good agreement with the numerical results. At the lowest drive the wave is essentially completely transmitted: the reflected component is very small and almost entirely consisting of the second harmonic. Indeed, the linear theory results (23) and (24) predict 100% transmission and zero reflection for these conditions. Figure 4 is the pressure distribution in the layer at time $20\times2\pi/\omega$ for all six driving amplitudes; again, the line corresponding to $P_{\rm inc}/P_\infty=0.2$ is dotted and shows the incipience of shock formation.

The analog of Fig. 2, but at the much higher amplitude

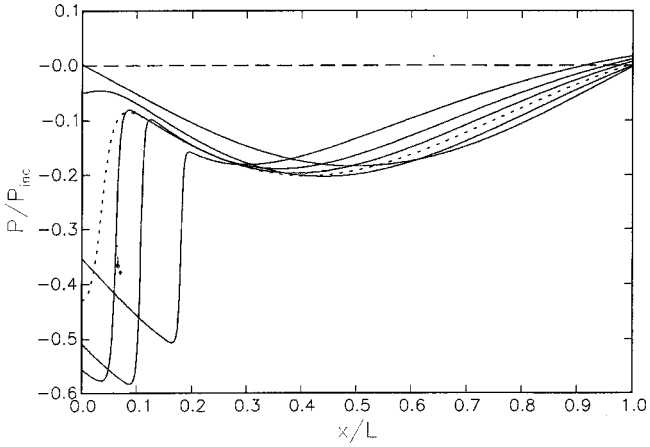

FIG. 4. Pressure field inside the bubble layer at time $20\times\omega/2\pi$ for different amplitudes of the incident wave, $P_{\rm inc}/P_\infty=0.01$, 0.1, 0.2 (dotted), 0.3, 0.5, 0.9 according to the quasi-equilibrium model. The frequency of the incident wave is equal to the first linear eigenfrequency of the layer $\omega=\omega_1$, with $\omega_1/2\pi=1.347$ kHz. The gas volume fraction is $\beta_0=0.133\%$; other conditions as specified at the beginning of Sec. V.

$P_{\rm inc}/P_\infty=0.7$, is shown in Fig. 5. The circles and squares connected by dashed lines are the numerical results while the solid and dotted lines show the linear theory predictions. Now that the threshold value is far exceeded, nonlinear effects are dominant, and the discrepancy between the two sets of results is very pronounced, especially when the incident frequency is close to the first linear eigenfrequency of the layer, $\omega/\omega_1\sim1$. The maximum of the resonance curve of the transmitted wave is about 0.6, rather than 1, and it occurs at a value of ω/ω_1 shifted to the left of the linear resonance condition, which indicates the expected softening behavior of the nonlinear oscillator. The considerable dissipation seen in this case is a consequence of shock formation in the layer.

The transient process that culminates in the formation of

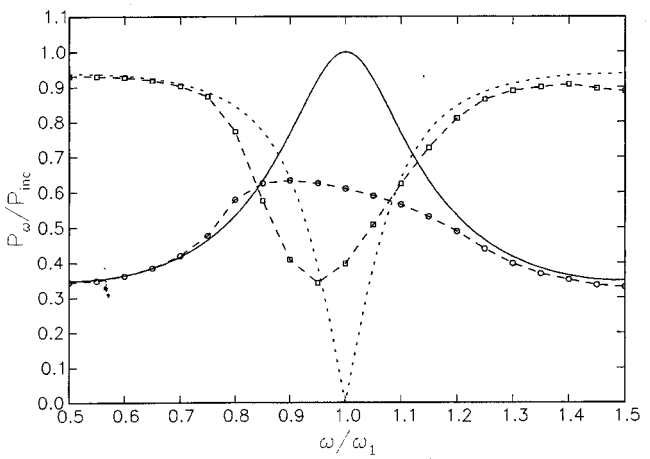

FIG. 5. Pressure amplitudes of the component at the incident wave frequency ω for the transmitted (circles) and reflected (squares) waves as functions of the incident frequency ω normalized by the first linear eigenfrequency of the layer according to the quasi-equilibrium model, $\omega_1/2\pi=1.347$ kHz. The dashed lines connecting circles and squares are only guides to the eye. The solid and dotted lines are the linear results given in Eqs. (23) and (24). The incident wave amplitude $P_{\rm inc}/P_\infty=0.7$ is greater than the threshold value for shock formation given by (38). The gas volume fraction is $\beta_0=0.133\%$; other conditions as specified at the beginning of Sec. V.

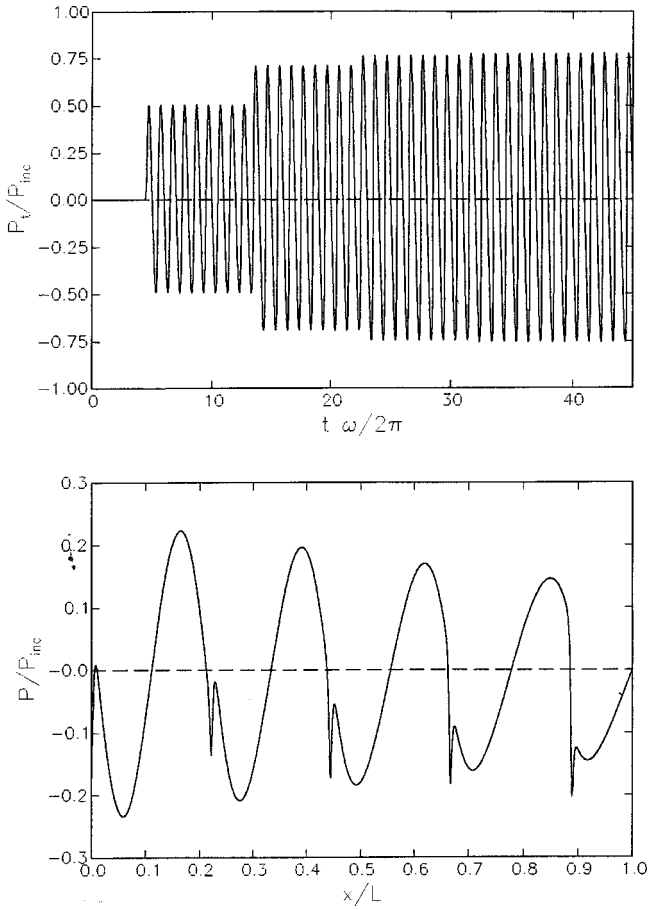

FIG. 6. Transmitted wave (upper panel) and pressure field inside the bubble layer at time $t=45\times 2\pi/\omega$ for $P_{\rm inc}/P_\infty=0.05$, $\beta_0=0.133\%$, and $\omega=9\omega_1=2\pi\times 12.1$ kHz according to the quasi-equilibrium model.

a shock is due to the gradual build-up of the multiple reflections that occur at the layer boundaries and is demonstrated in Fig. 6. The upper panel shows, as a function of the normalized time $\omega t/2\pi$, the normalized transmitted wave, which is seen to be progressively reinforced each time the shock developing inside the bubbly layer reflects at the layer boundary at $x=L$. Here the frequency of the incident wave is equal to the ninth linear eigenfrequency of the layer, $\omega/\omega_1=9$, and the polytropic index equals 1. The incident wave has amplitude $P_{\rm inc}/P_\infty=0.05$ and thus exceeds the threshold value (38) which, for these conditions, is 0.02. The time needed for the wave to travel from the left boundary $x=0$ to $x=L$ and back is about $9\times 2\pi/\omega$, and this is the approximate time separation of the steps that are clearly seen in the first few reflections. The lower panel of the figure shows the pressure field inside the layer at the end of the calculation shown in the upper panel, $45\times 2\pi/\omega$. The steady-state shape of the transmitted wave is shown in Fig. 7, with a clearly evident shock structure as expected.

The results of Figs. 6 and 7 should be compared with those presented in Fig. 3 of Druzhinin *et al.* (1996). The numerical scheme used in that work introduced numerical dispersion due to the discretization, which led to oscillations near the shock. By testing their code we realized that these oscillations are sensitive to the spatial step used in the calculation, and must therefore be considered an artifact of the numerical method used.

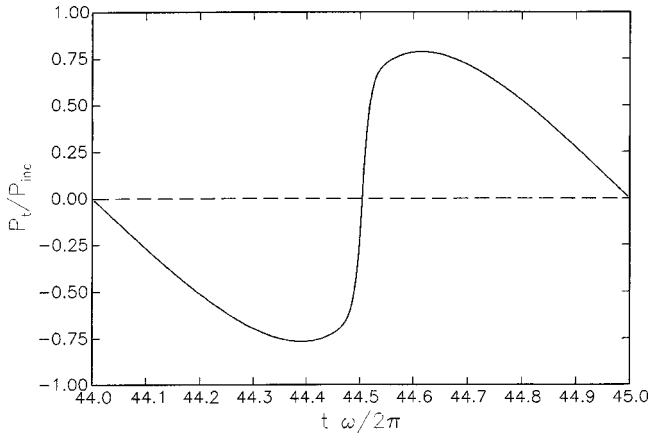

FIG. 7. Steady-state shape of the transmitted wave for the case of Fig. 6 ($P_{\rm inc}/P_\infty=0.05, \beta_0=0.133\%, \omega=9\omega_1$) according to the quasi-equilibrium model.

B. Complete model

We now turn to the complete model in which the bubble behavior is described by Eqs. (5)–(7). The inertia affecting the bubble pulsations now causes a strong dependence of the pressure wave upon the bubble radius, and thermal effects contribute to the damping of the wave. Thus, it is interesting to compare the predictions of this model with those of the polytropic approximation (which includes inertia but no thermal damping) and of the quasi-equilibrium model (which includes neither).

In choosing a suitable value of the polytropic index for use with the polytropic model we face the usual problem of the lack of a basis for this choice when the gas is neither clearly adiabatic nor isothermal. In our calculations we use for κ_p the linear-theory value κ_l defined in (17). Note that κ_l and ω_0 as given by the linearized theory of Sec. (III) depend on the driving frequency; the values that we quote below are calculated for the driving frequency of the incident wave ω.

In order to illustrate the effect of the bubble radius we consider the response of a layer driven near its first mode for two cases, both with the same gas volume fraction, $\beta_0=0.133\%$, but with a different radius of the constituent bubbles, $R_0=0.121$ and 1.21 mm. Again, the isothermal linear frequency of the lowest layer mode, according to (26), is $\omega_1/2\pi=1.347$ kHz.

In the first case the bubble equilibrium radius is $R_0=0.121$ mm; the linear bubble resonance frequency, 23.27 kHz, is thus much greater than that of the layer mode. With $\omega=\omega_1$ the linear polytropic index of the bubbles as given by (17) is $\kappa_l=1.035$, which confirms the essentially isothermal behavior of the gas.

Figure 8 shows the transmitted wave at steady state normalized by the amplitude of the incident wave as a function of the dimensionless time $t\omega/2\pi$ for two incident amplitudes, $P_{\rm inc}/P_\infty=0.01$ (upper panel) and $P_{\rm inc}/P_\infty=0.7$ (lower panel). The solid lines are the results of the complete model, while the dotted and dashed lines are the results for the polytropic and quasi-equilibrium models with $\kappa_p=1$, respec-

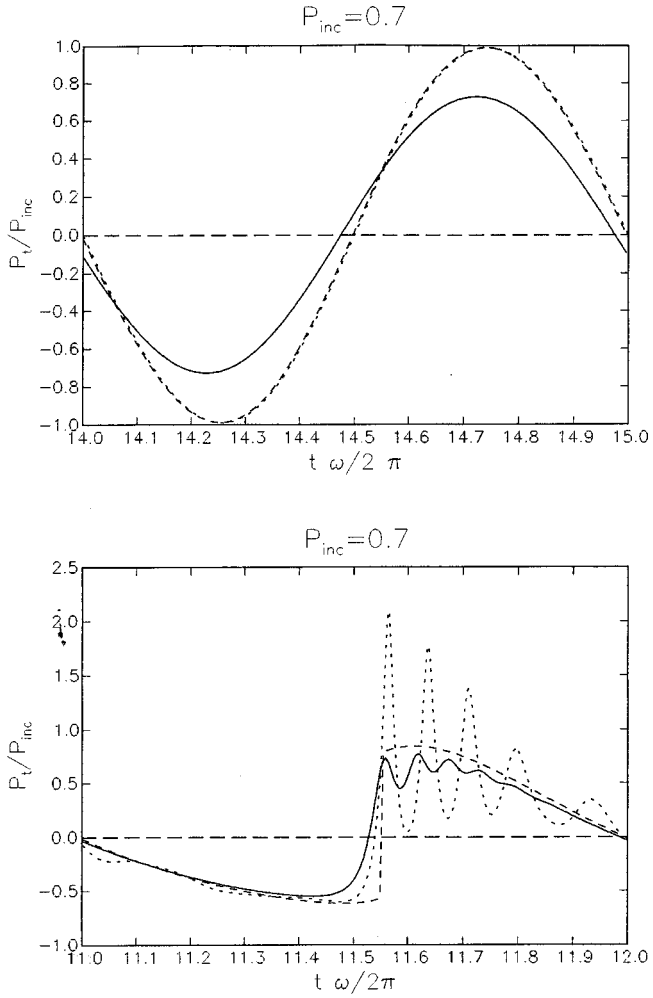

FIG. 8. Steady-state shape of the transmitted wave according to the complete model (solid line), compared with polytropic (dotted line) and quasi-equilibrium (dashed line) models with $\kappa_p=1$; upper panel $P_{\rm inc}/P_\infty=0.01$, lower panel $P_{\rm inc}/P_\infty=0.7$; $\omega/2\pi=1.347$ kHz, $\beta_0=0.133\%$, $R_0=0.121$ mm.

tively. When the incident amplitude is small (upper panel) the polytropic and quasi-equilibrium models give essentially the same result, which is expected in this case in which the incident frequency is much smaller than the bubble resonance frequency. The complete model predicts a somewhat smaller amplitude and a small phase shift, both due to the inclusion of thermal dissipation in the bubble motion, but behaves otherwise very similarly. In principle, these features contain information about the bubble size and possibly other quantities, although its extraction might be problematic in practice.

For the larger-amplitude excitation (lower panel of Fig. 8) all three models predict shock formation, but the differences among them are more pronounced. The complete model (solid line) shows a transmitted wave with slight oscillations near the maximum, while these oscillations are highly exaggerated by the polytropic model (dotted line). The same qualitative difference is encountered when the two models are applied to shock waves in bubbly liquids (Watanabe and Prosperetti, 1994). Since these oscillations are a consequence of bubble inertia, their absence in the quasi-equilibrium model (dashed line) is not surprising. The reason

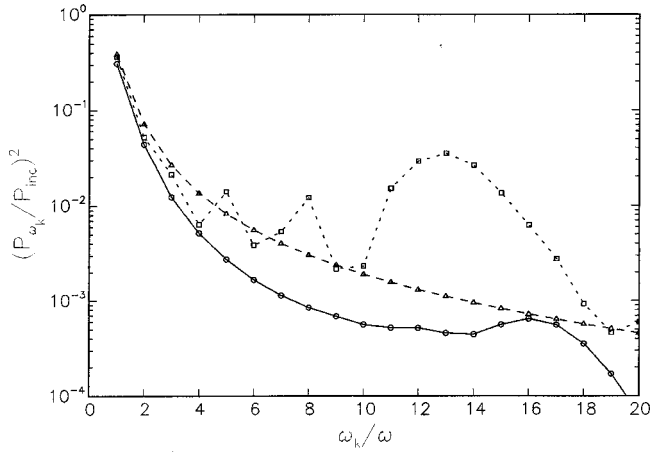

FIG. 9. Power spectrum of the transmitted wave for the case of the lower panel of Fig. 8 according to the complete model (circles), compared with polytropic (squares) and quasi-equilibrium (triangles) models with $\kappa_p=1$; $P_{\rm inc}/P_\infty=0.7$, $\omega/2\pi=1.347$ kHz, $R_0=0.121$ mm. The lines are only guides to the eye.

why this feature is encountered at this higher amplitude but not at the lower amplitude of the upper panel of Fig. 8 is that the formation of the shock introduces a much shorter characteristic time scale in the wave, which is not too far from the resonant period of the bubbles. Due to the absence of thermal effects, the polytropic model is less dissipative than the complete one, and the shock time scale is accordingly shorter: the smaller damping and the shorter time scale combine to cause the prominent oscillations of the result. If these oscillations are averaged out in the mind's eye, one sees a substantial similarity among the different profiles which is due to the fact that the underlying, relatively slowly varying, wave structure is only slightly damped in all models. In any event, it may be noted that the high-frequency oscillations of the complete model are so strongly damped that the quasi-equilibrium model ends up being a better approximation to the actual behavior than the polytropic model.

The power spectrum of the transmitted wave for $P_{\rm inc}/P_\infty=0.7$ is shown in Fig. 9. The circles represent the complete model, the squares the polytropic model, and the triangles the quasi-equilibrium model; the lines connect the symbols as an aid to the eye. The more dissipative nature of the complete model is evident from this comparison, as expected. The polytropic model exhibits several peaks corresponding to the harmonics of the drive and reflecting the strong oscillations of the lower panel of Fig. 8; these features are caused by the strongly nonlinear bubble response. The complete model, instead, only shows a mild resonance in correspondence with the bubble fundamental resonance at $\omega/\omega_1\simeq 16$.

In order to illustrate the behavior of the layer when the bubble natural frequency is not as different from the layer modal frequency as in the previous case, we consider now bubbles with an equilibrium radius of 1.21 mm, for which $\omega_0/2\pi=2.647$ kHz and $\kappa_l=1.35$. In this case the bubble natural frequency is about twice that of the lowest eigenmode of the layer.

Figure 10 shows the components of the transmitted (upper panel) and reflected (lower panel) waves at the incident

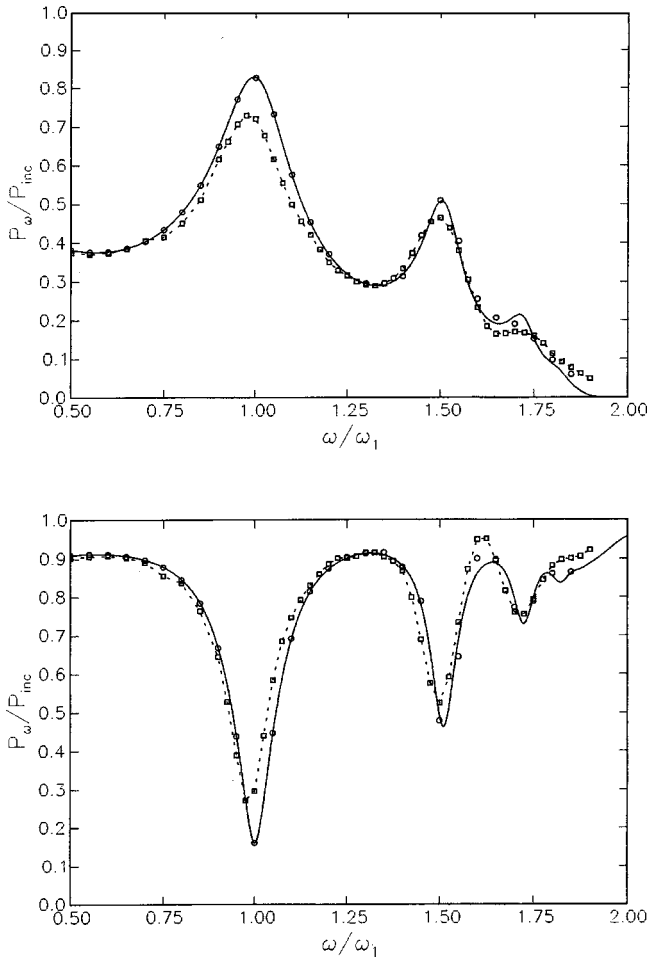

FIG. 10. Pressure amplitudes of the component at the incident wave frequency ω for the transmitted (upper panel) and reflected (lower panel) waves as functions of the incident frequency ω normalized by the first quasi-equilibrium linear eigenfrequency of the layer, $\omega_1/2\pi=1.347$ kHz. The circles and squares are the numerical results of the complete model for amplitudes $P_{\rm inc}/P_\infty=0.05$ and $P_{\rm inc}/P_\infty=0.7$, respectively. The solid curves are the linear results given by (21) and (22). The dotted lines connecting squares are only guides to the eye. The bubble radius is 1.21 mm.

frequency for $P_{\rm inc}/P_\infty=0.05$ (circles) and $P_{\rm inc}/P_\infty=0.7$ (squares) according to the complete model as functions of the normalized incident frequency ω/ω_1, with $\omega_1/2\pi=1.347$ kHz as before; the dotted lines connect the symbols as an aid to the eye. The lower-amplitude results match very well the analytic linear results of (21) shown by the solid line. Remarkably, when normalized by the incident pressure as here, the higher-amplitude results are only slightly different, with somewhat less pronounced maxima and minima and a slight shift to lower frequencies. This is surprising in view of the earlier results shown in Fig. 5, where a much greater difference was encountered. The explanation lies in the fact that shock formation in that case caused a strong energy dissipation that is absent in the complete-model results of Fig. 10.

The frequency range in Fig. 10 is near the bubble resonance where, for equal bubbles, the phase speed of pressure waves decreases substantially (see, e.g., Commander and Prosperetti, 1989). This circumstance has the effect of moving all the layer resonances to lower frequencies, the more

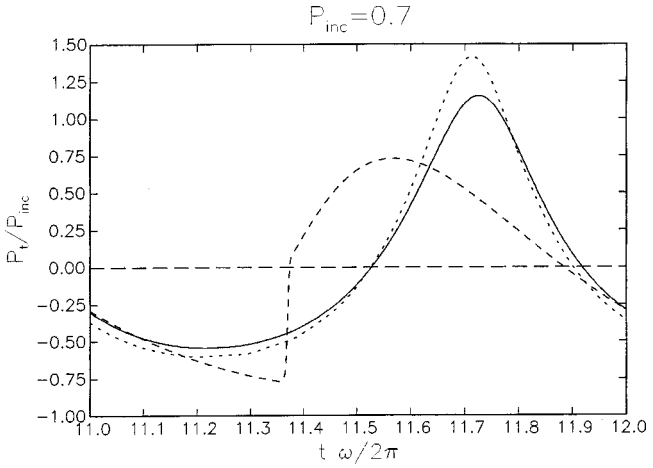

FIG. 11. Steady-state waveform of the transmitted wave for $P_{\rm inc}/P_\infty=0.7$ and $\omega/\omega_1=0.975$ according to the complete model (solid line), compared with polytropic (dotted line) and quasi-equilibrium (dashed line) models with $\kappa_p=1.35$; all conditions as in Fig. 10.

the closer they are to the bubble natural frequency: the decreasing spacing between maxima and minima with increasing frequency is evident from the figure. In the quasi-equilibrium model, on the other hand, the absence of dispersion gives an equal spacing between maxima and minima.

The transmitted waveforms near the first resonance, $\omega/\omega_1=0.975$, are shown in Fig. 11 for an incident wave amplitude $P_{\rm inc}/P_\infty=0.7$. In this case, in which the bubbles behave nearly adiabatically, the total damping is small and the complete (solid line) and polytropic (dotted line) model results are, accordingly, close; the dashed line is the quasi-equilibrium model, which shows an unrealistic shock structure that is eliminated by inertia in the other models.

The power spectrum of the transmitted wave is shown in Fig. 12. As compared with the previous case of Fig. 8, the spectrum for the complete model (circles) exhibits a much faster decay due to the fact that all these modes are above the fundamental bubble resonance; the polytropic result (squares) is similar, confirming that thermal damping effects

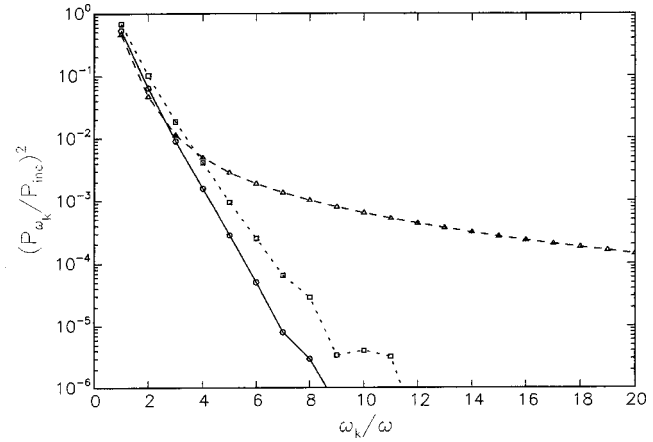

FIG. 12. Power spectrum of the transmitted wave for the case of Fig. 11 according to the complete model (circles), compared with polytropic (squares) and quasi-equilibrium (triangles) models with $\kappa_p=1.35$. The lines are only guides to the eye.

are small, while the quasi-equilibrium model spectrum (triangles) decays much more slowly due to the presence of the shock.

VI. RESULTS: DUAL-FREQUENCY EXCITATION

We now consider the behavior of the bubble layer when the incident wave contains two frequencies, $\omega^{(1)}$ and $\omega^{(2)}$. The nonlinearity will then produce several Fourier components and in particular the difference frequency $\Omega=\omega^{(2)}-\omega^{(1)}$. By arranging for both incident frequencies and the difference frequency to correspond to normal modes of the layer, an effective generation of the low-frequency component may be expected to take place.

In order to avoid the strong damping that has plagued earlier attempts to use bubbly liquids in parametric arrays, it is important to operate under conditions in which the bubble natural frequency is higher than either incident frequency. As noted before in Sec. II, this condition corresponds to the assumptions that justify the quasi-equilibrium model of Eq. (9) with $\kappa_p=1$ and, for this reason, we start the study of the low-frequency signal generation with this model. Except where explicitly noted, the parameters used in the calculations have the same value as given at the beginning of Sec. V.

We consider a bubble layer excited by a biharmonic incident wave with components at frequencies $\omega^{(1)}$ and $\omega^{(2)}$ close to the ninth and tenth eigenmodes of the layer; for all cases considered in this section both incident components have the same amplitude $P_{\rm inc}$, $A^2=31$, and $\kappa_p=1$. In order to operate much below the bubble resonance frequency, we increase the thickness of the layer to $L=0.4$ m; for isothermal conditions the frequency of the fundamental model is $\omega_1/2\pi=0.337$ kHz.

A typical example of the steady-state shape of the transmitted wave is shown in the upper panel of Fig. 13 where $\omega^{(1)}=9\omega_1=2\pi\times3.03$ kHz and $\omega^{(2)}=10\omega_1=2\pi\times3.37$ kHz, so that the difference frequency equals the first eigenfrequency of the layer, $\omega_1=0.337$ kHz, providing the resonance conditions for the low-frequency signal. The amplitude of each one of the incident components is $P_{\rm inc}/P_\infty=0.5$. In addition to the nonlinearly generated low-frequency component, the slow modulation of the waveform reflects the standard beats due to the superposition of two oscillations with close periods (the same phenomenon is visible in Fig. 17 below). The pressure field inside the bubble layer at the times $t=8\times2\pi/\omega_1$ and $t=8.5\times2\pi/\omega_1$ is shown in the lower panel of Fig. 13. Since the amplitude of the incident wave is much larger than the threshold value for shock formation (equal to 0.02 for this case), shocks form in the layer and are reflected at the boundaries, which is responsible for the characteristic double shock-front structure present in the pressure field in the lower panel of Fig. 13. The internal shocks confer a sawtooth structure to the transmitted wave as shown in the upper panel of Fig. 13. The relative power of the difference-frequency harmonic in the transmitted wave, i.e., $(P_\Omega/P_{\rm inc})^2$, is 1.12×10^{-2}.

The dependence of the low-frequency output on the incident frequencies is shown in Fig. 14 where the pump frequencies $\omega^{(1)}$ and $\omega^{(2)}$ are changed in such a way that the difference-frequency is fixed and equal to the layer first eigenfrequency, $\Omega=\omega^{(2)}-\omega^{(1)}=\omega_1$. The circles, squares,

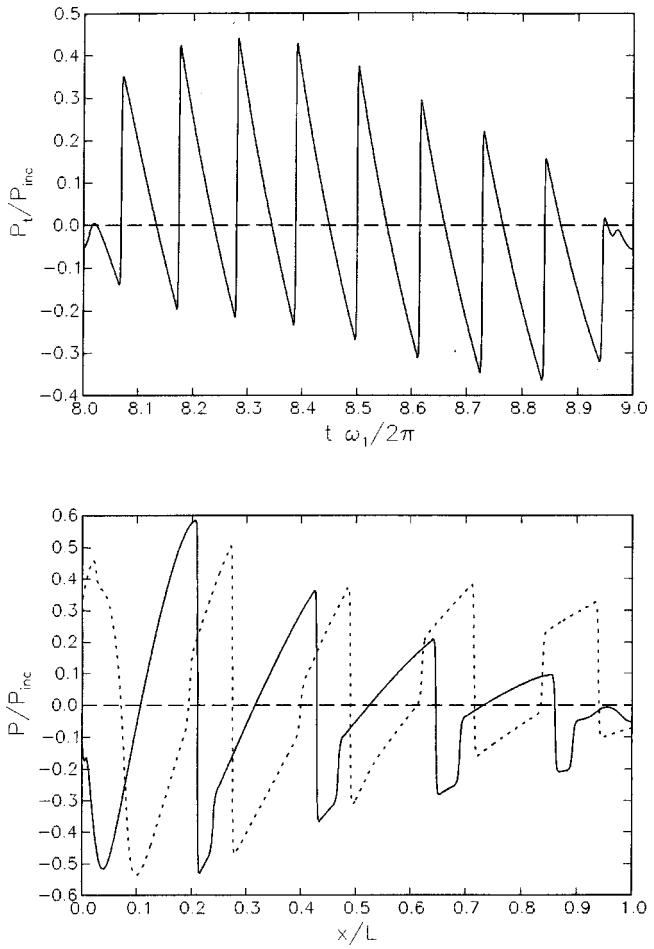

FIG. 13. Steady-state shape of transmitted wave (upper panel) produced by the quasi-equilibrium model and pressure field inside the bubble layer at time $t=8\times2\pi/\omega_1$ (solid line) and $t=8.5\times2\pi/\omega_1$ (dotted line) for dual-frequency excitation with $\omega^{(1)}=9\omega_1=2\pi\times3.03$ kHz, $\omega^{(2)}=10\omega_1=2\pi\times3.37$ kHz and amplitude $P_{\rm inc}/P_\infty=0.5$.

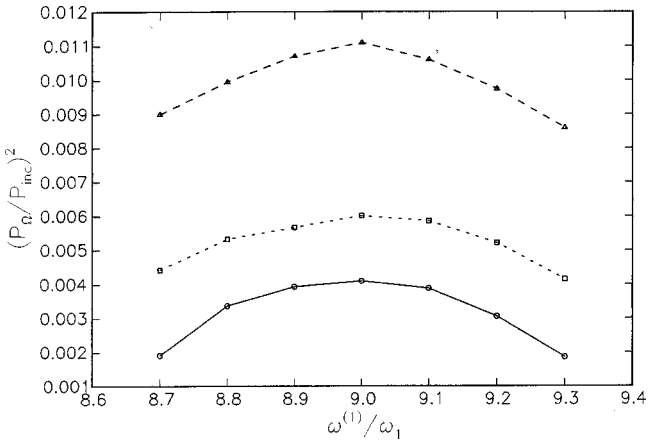

FIG. 14. Relative power of the low-frequency component in the transmitted wave according to the quasi-equilibrium model for dual-frequency excitation as a function of $\omega^{(1)}$ with $\omega^{(2)}=\omega^{(1)}+\omega_1$. The circles, squares, and triangles are the results for $P_{\rm inc}/P_\infty=0.1$, 0.2, and 0.5 respectively. The lines are only guides to the eye.

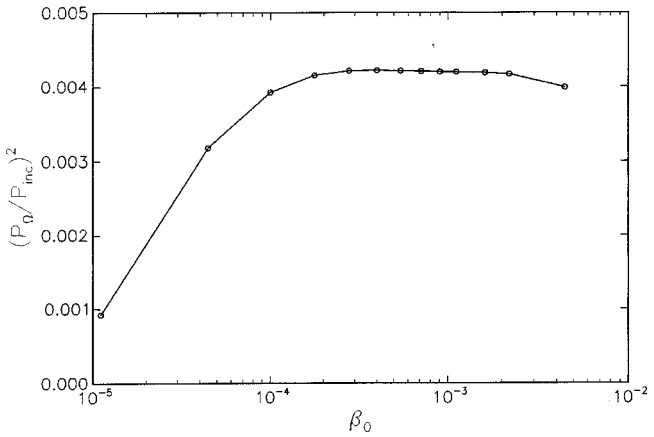

FIG. 15. Relative power of the low-frequency component predicted by the quasi-equilibrium model for dual-frequency excitation as a function of the gas volume fraction in the layer; $\omega^{(1)}=9\omega_1=2\pi\times3.03$ kHz, $\omega^{(2)}=10\omega_1=2\pi\times3.37$ kHz, and $P_{inc}/P_\infty=0.1$.

and triangles are the results for $P_{inc}/P_\infty=0.1$, 0.2, and 0.5, respectively. The lines are only guides to the eye. As expected, the relative power of the low-frequency signal has a maximum around $\omega^{(1)}=9\omega_1$ when both pump frequencies are at resonance conditions.

Figure 15 shows the relative low-frequency transmitted power as a function of the parameter β_0 for $P_{inc}/P_\infty=0.1$, again for the quasi-equilibrium model. With increasing gas volume fraction, the amplitude of the difference-frequency transmitted wave quickly saturates to an approximately constant value, after which it begins to decline. We have found that, in order to obtain converged results, the number of grid points had to be increased to 6400 at the higher volume fractions. For example, the difference between the values of $(P_\Omega/P_{inc})^2$ as computed with 3200 or 6400 points is 2.4% for $\beta=1.11\times10^{-3}$, and increases to 5.8% for $\beta=2.84\times10^{-3}$.

Figure 16 shows the relative power of the low-frequency signal $(P_\Omega/P_{inc})^2$ of the transmitted (circles) and reflected (squares) waves as a function of the amplitude of the incident wave components P_{inc}/P_∞ when $\omega^{(1)}=9\omega_1$ and $\omega^{(2)}=10\omega_1$; the solid and dotted lines are for the complete model while the dot-dash and dashed lines are for the quasi-equilibrium model. Here the bubble radius is $R_0=50$ μm, with a linear resonance frequency $\omega_0/2\pi=55.86$ kHz and $\kappa_l=1.01$.

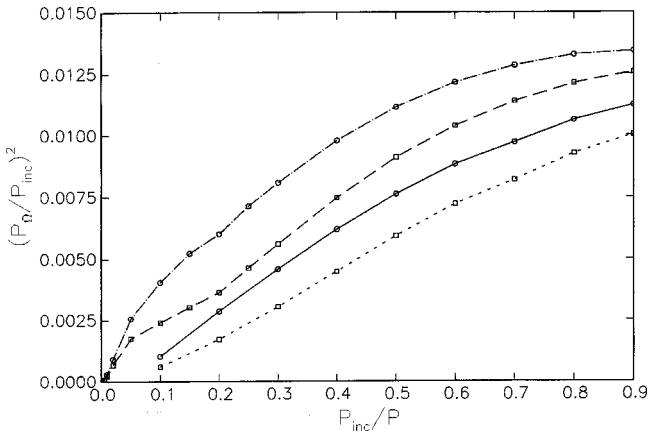

FIG. 16. Relative power of the low-frequency component in the transmitted (circles) and reflected (squares) waves for dual-frequency excitation as a function of the amplitude P_{inc}/P_∞ of the incident wave components for $\omega^{(1)}=9\omega_1=2\pi\times3.03$ kHz and $\omega^{(2)}=10\omega_1=2\pi\times3.37$ kHz. The lines are only guides to the eye. The solid and dotted lines are for the complete model while the dot-dash and dashed lines are for the quasi-equilibrium model with $\kappa_p=1$. The bubble radius is 50 μm.

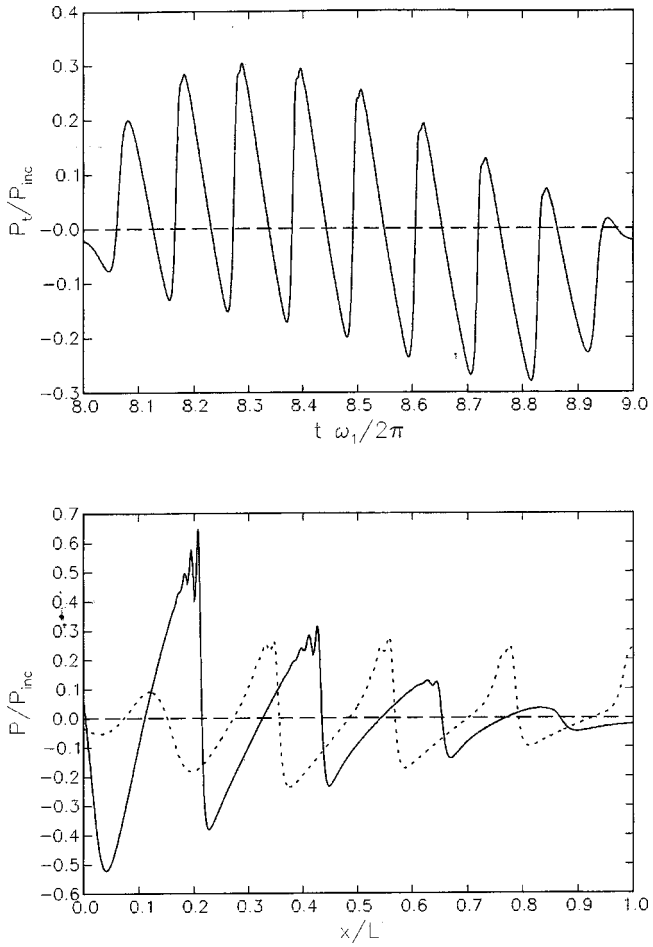

FIG. 17. Steady-state shape of transmitted wave (upper panel) produced by the complete model and pressure field inside the bubble layer at times $t=8\times2\pi/\omega_1$ and $t=8.5\times2\pi/\omega_1$ for dual-frequency excitation with $\omega^{(1)}=9\omega_1=2\pi\times3.03$ kHz, $\omega^{(2)}=10\omega_1=2\pi\times3.37$ kHz, and amplitude $P_{inc}/P_\infty=0.5$. These results should be compared with those given by the quasi-equilibrium model presented in Fig. 13.

The relative power of the low-frequency signal increases with the amplitude of the incident wave, but the proportionality to the square of the incident wave amplitude predicted by the weakly nonlinear theory (Druzhinin *et al.*, 1996) is found only for small amplitudes, $P_{inc}/P_\infty\leqslant0.01$, and is not apparent from this figure. The quasi-equilibrium-model results of Fig. 16 are much lower than the numerical results presented in Figs. 6(a) and (b) of Druzhinin *et al.* (1996), apparently once again due to numerical artifacts of that work.

Figure 17 shows the steady-state temporal transmitted waveform (upper panel) and the pressure field inside the bubble layer at time $t=8\times2\pi/\omega_1$ for $\omega^{(1)}=9\omega_1$, $\omega^{(2)}=10\omega_1$, $P_{inc}/P_\infty=0.5$, for 50-μm-radius bubbles. This figure should be compared with Fig. 13 for the quasi-equilibrium model. The transmitted wave still has a sawtooth

TABLE I. Relative power of the transmitted and reflected waves produced by the complete model for a dual-frequency incident wave with $\omega^{(1)}=9\omega_1$, $\omega^{(2)}=10\omega_1$, $P_{\rm inc}/P_\infty=0.1$; other conditions as given at the beginning, of Sec. V except that the layer thickness is 0.4 m ($\omega_1/2\pi=337$ Hz) and 0.1 m ($\omega_1/2\pi=1{,}347$ Hz).

R_0 (mm)	$\omega_0/2\pi$ (Hz)	κ_l	$\omega_1/2\pi$ (Hz)	(Transmitted power)/$\lvert P_{\rm inc}\rvert^2$		(Reflected power)/$\lvert P_{\rm inc}\rvert^2$	
				Total	At Ω	Total	At Ω
0.05	55,86	1.01	337.0	0.16	1.0×10^{-3}	0.77	6.1×10^{-4}
0.05	55,90	1.08	1,347	0.02	2.5×10^{-4}	0.95	1.7×10^{-4}
0.1	28,76	1.08	337.0	0.02	2.4×10^{-4}	0.97	1.6×10^{-4}
0.1	30,57	1.22	1,347	0.02	2.4×10^{-4}	0.94	1.6×10^{-4}
1	3,22	1.36	337.0	2.4×10^{-5}	2.4×10^{-5}	1.72	2.0×10^{-5}
1	3,24	1.38	1,347	0.20	2.5×10^{-6}	1.79	6.3×10^{-6}

appearance, but the peaks are less sharp, which is evidence of the stronger damping affecting the higher frequencies. Due to the increased dissipation, the shocks inside the layer are strongly damped before they reach the right end and their reflection there is thus less strong than before, which explains the marked differences between the lower panels of Figs. 17 and 13. Now oscillations near the back of the shock are present; these are related, as before, to bubble inertia. The relative power of the difference-frequency harmonic in the transmitted wave is 7.6×10^{-3}; for the same conditions, but at $P_{\rm inc}/P_\infty=0.1$, the relative power is 1.0×10^{-3}. The corresponding results for the quasi-equilibrium model are 11.2×10^{-3} and 4.05×10^{-3}, respectively, for $P_{\rm inc}/P_\infty=0.5$ and 0.1. In both cases the relative power of the transmitted difference-frequency predicted by the complete model is smaller than that of the quasi-equilibrium model.

The present problem contains a large number of parameters, and it is not practical to present an exhaustive investigation of the entire parameter space. Some further insight into the dependence of the low-frequency transmitted component on various quantities can be gained from Table I which summarizes the results of several calculations for different parameters of the layer and air bubbles. In all cases $A=\sqrt{31}$, and the layer is excited by a biharmonic wave at frequencies $\omega^{(1)}=9\omega_1$ and $\omega^{(2)}=10\omega_1$ with amplitude $P_{\rm inc}/P_\infty=0.1$. The bubble layer has a thickness of 40 cm ($\omega_1/2\pi=337$ Hz) and 10 cm ($\omega_1/2\pi=1{,}347$ Hz); $\kappa_p=\kappa_l$ is evaluated at $\omega^{(2)}$. These results show that the relative power of the low-frequency signal is larger when the frequencies of the incident wave are much smaller than the bubble resonance frequency and the bubble oscillations are isothermal. These conditions might suggest the use of the simpler quasi-equilibrium model; however, in all cases, we have found that the latter tends to overpredict the amplitude of the low-frequency signal.

VII. CONCLUSIONS

The results presented in this paper correct and expand the scope of the earlier ones of Druzhinin *et al.* (1996). In comparison with that work, we have used a more realistic description of the bubble behavior which includes the effects of radial inertia, with the associated dispersion, and of the gas thermal behavior, with the attendant energy losses. As expected, several details of the predictions of the earlier model are modified by these effects, although the basic character remains. Thus, we find a propensity for shock-wave generation in the bubbly layer which gives rise to a transmitted wave with a sawtooth character.

We have also studied the possibility of enhanced low-frequency difference-wave generation through the exploitation of the resonances of the bubbly layer. We have concluded that the estimates presented in our earlier work were excessively large due to a combination of the idealizations of the model and an insufficiently accurate numerical scheme. However, even after correction, we find that a difference-wave power of the order of 1% of the incident power (Fig. 16) can be generated using incident wave amplitudes of less than 100 kPa. Thus, this technique for the parametric generation of low-frequency waves may have practical value.

An important aspect of the phenomenon, confirmed by this study, is that operation near the resonance frequency of the individual bubbles is detrimental to the energy conversion efficiency due to the strong dissipation of the bubble motion in this frequency range.

In order to avoid the practical difficulties connected with the generation and control of suitable bubbles, it might be expedient to apply the principle described in this paper to other systems. For example, one would expect similar phenomena to occur in porous waterlike (or rubberlike) media in which the shear modulus is small and plays the role of gas compressibility in bubbles; some experiments of this type are reported in Belyaeva and Timanin (1991). Like bubbles, pores in such media provide very strong nonlinearity (see, e.g., Naugolnykh and Ostrovsky, 1998, Sec. 1.4). At the same time, it is much easier to have small and almost equal-size pores, the system is more stable, and losses are typically smaller.

ACKNOWLEDGMENTS

The authors express their gratitude to the Office of Naval Research for the support of this work.

Akhatov, I., Parlitz, U., and Lauterborn, W. (**1994**). ''Pattern formation in acoustic cavitation,'' J. Acoust. Soc. Am. **96**, 3627–3635.

Belyaeva, I., and Timanin, E. (**1991**). ''Experimental study of the nonlinear properties of porous elastic media,'' Sov. Phys. Acoust. **37**, 533–544.

Caflisch, R. E., Miksis, M. J., Papanicolaou, G., and Ting, L. (**1985**). ''Effective equations for wave propagation in bubbly liquids,'' J. Fluid Mech. **153**, 259–273.

Carstensen, E. L., and Foldy, L. L. (**1947**). ''Propagation of sound through a liquid containing bubbles,'' J. Acoust. Soc. Am. **19**, 481–501.

Clay, C. S., and Medwin, H. (**1977**). *Acoustical Oceanography* (Wiley, New York).
Colonius, T., d'Auria, F., and Brennen, C. E. (**2000**). ''Acoustic saturation in bubbly cavitating flow adjacent to an oscillating wall,'' Phys. Fluids **12**, 2752–2761.
Commander, K. W., and Prosperetti, A. (**1989**). ''Linear pressure waves in bubbly liquids: comparison between theory and experiments,'' J. Acoust. Soc. Am. **85**, 732–746.
d'Agostino, L., and Brennen, C. E. (**1988**). ''Acoustical absorption and scattering cross-sections of spherical bubble clouds,'' J. Acoust. Soc. Am. **84**, 2126–2134.
Druzhinin, O. A., Ostrovsky, L. A., and Prosperetti, A. (**1996**). ''Low-frequency acoustic wave generation in a resonant bubble layer,'' J. Acoust. Soc. Am. **100**, 3570–3580.
Feng, Z. C., and Leal, L. G. (**1997**). ''Nonlinear bubble dynamics,'' Annu. Rev. Fluid Mech. **29**, 201–243.
Gasenko, V. G., Nakoryakov, V. E., and Shreiber, I. R. (**1979**). ''Nonlinear disturbances in a liquid containing gas bubbles,'' Sov. Phys. Acoust. **25**, 385–388.
Harten, A. (**1983**). ''High resolution schemes for hyperbolic conservation laws,'' J. Comput. Phys. **49**, 357–393.
Kamath, V., and Prosperetti, A. (**1989**). ''Numerical integration methods in gas-bubble dynamics,'' J. Acoust. Soc. Am. **85**, 1538–1548.
Kamath, V., Prosperetti, A., and Egolfopoulos, F. (**1993**). ''A theoretical study of sonoluminescence,'' J. Acoust. Soc. Am. **94**, 248–260.
Kogarko, B. S. (**1964**). ''One-dimensional unsteady motion of a liquid with an initiation and progression of cavitation,'' Dokl. Akad. Nauk SSSR **155**, 779–782 (in Russian).
Kustov, L. M., Nazarov, V. E., Ostrovsky, L. A., Sutin, A. M., and Zamolin, S. V. (**1982**). ''Parametric acoustic radiation with a bubble layer,'' Acoust. Lett. **6**, 15–17.
Kuznetsov, V. V., Nakoryakov, V. E., Pokusaev, G., and Shreiber, I. R. (**1978**). ''Propagation of perturbations in a gas-liquid mixture,'' J. Fluid Mech. **85**, 85–96.
Medwin, H., and Clay, C. S. (**1997**). *Fundamentals of Ocean Acoustics* (Morgan Kauffman, San Francisco).
Naugolnykh, K., and Ostrovsky, L. (**1998**). *Nonlinear Wave Processes in Acoustics* (Cambridge U.P., Cambridge, UK), Chap. 1, pp. 25–30.
Nigmatulin, R. I. (**1991**). *Dynamics of Multiphase Media* (Hemisphere, Washington), Vol. 1, Chap. 1, pp. 98–113.
Omta, R. (**1987**). ''Oscillations of a cloud of small bubbles of small and not so small amplitude,'' J. Acoust. Soc. Am. **82**, 1018–1033.
Ostrovsky, L. A., Sutin, A. M., Soustova, I. A., and Matveyev, A. I. (**1998**). ''Nonlinear, low-frequency sound generation in a bubble layer: Theory and laboratory experiments,'' J. Acoust. Soc. Am. **104**, 722–726.
Pierce, A. D. (**1989**). *Acoustics* (Acoustical Society of America, Woodbury, NY), Chap. 3, pp. 130–140.
Plesset, M. S., and Prosperetti, A. (**1977**). ''Bubble dynamics and cavitation,'' Annu. Rev. Fluid Mech. **9**, 145–185.
Prosperetti, A. (**1984**). ''Bubble phenomena in sound fields: Part one,'' Ultrasonics **22**, 69–77.
Prosperetti, A. (**1991**). ''The thermal behaviour of oscillating gas bubbles,'' J. Fluid Mech. **222**, 587–616.
Prosperetti, A. (**2001**). ''Fundamental acoustic properties of bubbly liquids,'' in *Handbook of Elastic Properties of Solids, Liquids, and Gases*, edited by M. Levy, H. E. Bass, and R. Stern (Academic, New York), Vol. 4, pp. 183–205.
Prosperetti, A., and Lezzi, A. (**1986**). ''Bubble dynamics in a compressible liquid. Part 1. First-order theory,'' J. Fluid Mech. **185**, 289–321.
Twersky, V. (**1962**). ''On scattering of waves by random distributions. I. Free-space scatterer formalism,'' J. Math. Phys. **3**, 700–715.
van Wijngaarden, L. (**1968**). ''On the equations of motion for mixtures of liquid and gas bubbles,'' J. Fluid Mech. **33**, 465–474.
Watanabe, M., and Prosperetti, A. (**1994**). ''Shock waves in dilute bubbly liquids,'' J. Fluid Mech. **274**, 349–381.
Waterman, P. C., and Truell, R. (**1961**). ''Multiple scattering of waves,'' J. Math. Phys. **2**, 512–537.
Zabolotskaya, E. A. (**1977**). ''Two self-action mechanisms for sound waves propagating in a gas-liquid mixture,'' Sov. Phys. Acoust. **23**, 338–340.
Zabolotskaya, E. A., and Soluyan, S. I. (**1973**). ''Emission of harmonic and combination frequency waves by air bubbles,'' Sov. Phys. Acoust. **18**, 396–398.
Zhang, D. Z., and Prosperetti, A. (**1994**). ''Ensemble phase-averaged equations for bubbly flows,'' Phys. Fluids **6**, 2956–2970.